Large Eddy Simulation of Flow around Circular Cylinders on Structured and Unstructured Grids, II

J. Fröhlich[1], W. Rodi[1], J.P. Bertoglio[2], U. Bieder[3], H. Touil[2]

[1] Inst. für Hydromechanik, Universität Karlsruhe, 76128 Karlsruhe, Germany

[2] LMFA, URA CNRS 263, Ecole Centrale de Lyon, 69131 Ecully, France

[3] CEA–Grenoble, 17 rue des Martyrs, 38054 Grenoble, France

Dedicated to R. Peyret

Summary

The paper presents LES computations of subcritical flow around circular cylinders. Uniform upstream conditions have been investigated with $Re = 3900$ and $Re = 140000$. The first case is considered for comparison between results obtained by the authors from earlier structured and unstructured computations and new results from a recently developed unstructured French code. Spanwise shear modifies the flow in substantial points and has been considered at $Re = 6250$. Time signals have been recorded and analyzed by means of Fourier and wavelet techniques. These reveal important differences between the flow with and without shear. Furthermore, work on the LES methodology is reported. We present a model for the laminar boundary layer employing an integral method and discuss the impact of streamwise variations of the grid on the computed resolved flow.

1   Introduction

The present paper is a follow–up of [17] concerned with the second phase of a common research project between IFH Karlsruhe, EDF Chatou, and LMFA Lyon on LES for the flow around cylinders.

Several studies have shown that Large Eddy Simulation (LES) is an appropriate simulation technique for bluff body flows. It generally yields better results than Reynolds–averaged models and on the other hand is affordable also at high Reynolds numbers when a Direct Numerical Simulation is too costly. Reviews on the subject can be found in [33], [34]. The flow around a subcritical circular cylinder has been considered in several papers on LES starting with the seminal work in [3]. This type of flow, due to its transitional character, is very sensitive to even small disturbancies. This is well–known from experiments [45] and has also been highlighted from a numerical point of view by the recent grid–refinement studies in [22]. Hence, the configuration is a severe test case. It is presumably more difficult than most industrial applications in similar geometry where the upstream turbulence level is generally higher such as for the tube bundle flow investigated by means of an LES on unstructured grids in [36].

The present paper is outlined as follows: We first report on recent computations for the circular cylinder at $Re = 3900$ focusing on the application of the new unstructured code developed by the French partners. Subsequently, computations at higher Reynolds numbers are reported. We then outline new model boundary conditions particularly suited for bluff–body flows. Finally, the flow around a cylinder in uniform shear flow

is considered focusing on the analysis of the complicated wake structure by means of wavelet techniques.
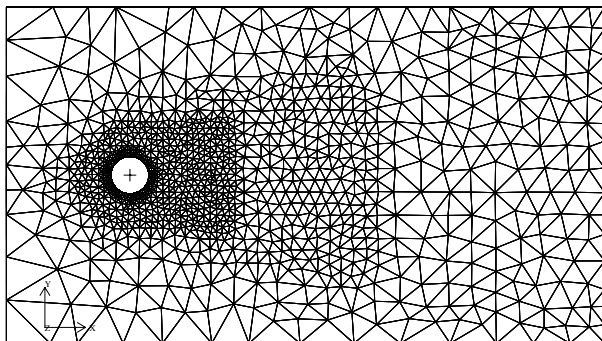

Figure 1 Cut in the $x - y$–plane through the unstructured grid with 300000 tetrahedra used for the computation with PRICELES.

2 Circular cylinder at $Re = 3900$

As an industrial partner, EDF experiences more than do academics the economical pressure on its research and development activities. This different attitude, with all its pros and cons, is one of the reasons for carrying out common research projects with partners from both areas to a mutual benefit. Recently, management as well as technical issues led EDF to abandon their code N3S for research on LES in favour of a new object–oriented Finite Element code, PRICELES (Platform Rapide Industrielle CEA EDF de LES) being developed together with CEA. At the same time the discretization scheme was revisited. This issue is more involved and less standardized with unstructured discretizations compared to structured or quasi–structured ones classically used for LES. Rollet–Miet et al. [36] proved that the P1/P1 element with suitable damping of oscillations is better suited for LES than classical Finite Elements. Further tests [5] however showed that in some cases a relatively fine grid is required to obtain satisfactory results. A new scheme was therefore developed, a P1–non-conforming/P1–bubble element, which mimics the staggered grid arrangement in structured Finite Volume codes [6].

The flow around a circular cylinder at $Re = 3900$ which had been computed with the structured Finite Volume code LESOCC [8] of IFH and N3S of EDF as reported in [17] was therefore revisited as one of the test cases for PRICELES [4]. Preliminary studies have shown that with PRICELES, more so than with N3S, regularity of the grid is an important issue. Hence, the previous Finite Element mesh was replaced by a new one with more degrees of freedom (600000 velocity nodes), lower aspect ratios, and smoother variation of the step size. A cross section is depicted in Fig. 1. Spanwise periodicity was replaced by a free–slip condition while increasing the respective extent of the calculation domain from $L_z = \pi$ to $L_z = 5$. (Note that everywhere in the present text distances are normalized with the cylinder diameter and velocities with the mean free–stream velocity.) All further characteristics were taken over from [17].
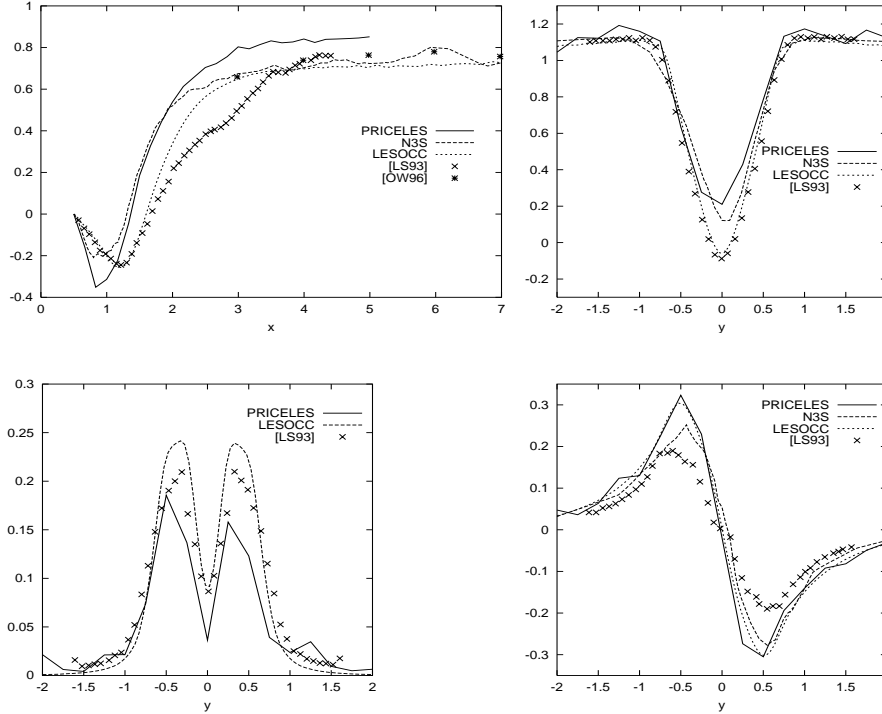
Figure 2 Cylinder flow at Re=3900: The new results obtained with PRICELES compared to the results of LESOCC and N3S (LRUN3 and NRUN1 in [17], respectively) as well as to the experimental data of [23] as reported in [3] and [27]. Top: Profiles of the mean streamwise velocity field at $y = 0$ (left) and $x = 1.54$ (right) Bottom: Profiles of the resolved fluctuations $\langle u'u' \rangle$ (left) and the mean normal velocity at $x = 1.54$ (right). The points where values from PRICELES were stored have no relation to the grid employed.

The computed instantaneous flow exhibits the features known from earlier computations and experiments such as [43]. Flow visualizations [4] show the typical vortex roll–up and braid–structures resulting from the formation of secondary spanwise vortices. The computation was performed for 7 shedding cycles, 3 of which were used for averaging. This amount is definitely too small for the statistics in the wake to converge with only some saturation close to the cylinder being observed. Nevertheless, important information on the behaviour of the code could be gained. Fig. 2 displays profiles of the average velocity field in the wake and for $\langle u'u' \rangle$ in comparison to the results in [17]. The recirculation length is obtained too short compared to the experiment [23]. In light of the discussion in [22] this is likely to result from insufficient resolution of the separating laminar shear layers and would certainly be improved by refining the grid in this region. In [22] it is even conjectured that the experiment of [23] suffered from disturbances and that ideally the recirculation region is larger reflecting a later transition of the shear layers.

Fig. 3 shows spectra from different LES of the considered flow as well as from the experiment of [27]. Fig. 3a taken from [24] illustrates the better representation of small scales when replacing an upwind scheme with a central scheme. Fig. 3b displays spectra from the computation with the structured Finite Volume code LESOCC using central differences, LRUN3 in [17], which have not been reported previously. It shows that with
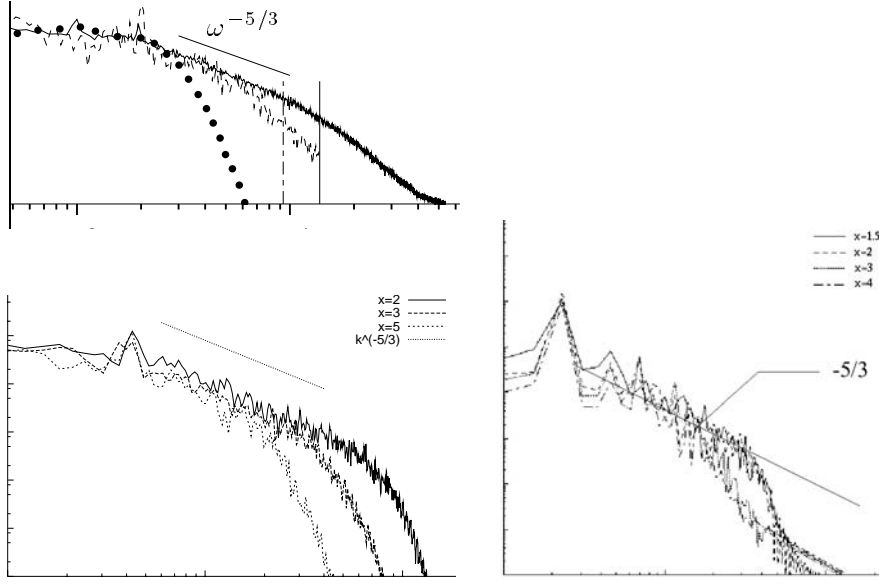
Figure 3 Spectra in the wake of the cylinder at $Re = 3900$ on the centerline. a) One–dimensional energy spectra E_{11} at $x = 5$ as compiled in [24]: − Experiment of [27], ● LES of [3] with upwind-biased scheme, - - - LES with central/Fourier scheme of [24]. b) E_{11} in the computation with LESOCC, LRUN3 of [17], at $x = 2,3,5$. c) Spectra of turbulent kinetic energy obtained with PRICELESS at $x = 1.5,2,3,4$ [4]. Note that for reasons of flow topology E_{11} exhibits a maximum at $2St$ while the kinetic energy has a maximum at St. Tic marks have been droped because of different normalization of the axes.

increasing distance from the cylinder in the wake the spectra decay faster. This is partly due to the physical decay of the turbulence as reported in [27] but mainly due to the coarsening of the grid in streamwise direction. The extent of the inertial range at $x = 5$ in LRUN3 is comparable to the one in [24]. Fig. 3c displays energy spectra from the computation with PRICELES discussed above. Since the grid is coarser, in particular beyond $x = 3$ (cf. Fig.1), the inertial range extends less far.

Table 1 Computations for the flow around a circular cylinder at $Re = 140000$.

	RUN1	RUN2	RUN3	Experiments
$N_r \times N_\theta \times N_z$	$166 \times 206 \times 64$	$166 \times 206 \times 64$	$182 \times 306 \times 96$	
L_z/D	1	4	4	
St	0.217	0.208	0.207	0.179 [9], 0.2 [37]
C_D	1.157	1.246	0.91	1.237 [9], 1.2 [37]
C_{bp}	−1.33	−1.40	−0.93	-1.21[9], -1.34[40]
θ_{sep}	93.5^o	89.7^o	88.6^o	$79^o \pm 1^o$ [39]
L_r/D	0.42	0.59	0.70	0.5 ± 0.05 [9]

3 Circular cylinder at $Re = 140000$

The computation of the cylinder flow at $Re = 140000$ is substantially more demanding than at the lower Reynolds number considered before. The flow is subcritical, just below the drag crisis, so that the thin laminar boundary layer has to be resolved if a no–slip condition is applied. Since the boundary layer thickness is proportional to $\sqrt{Re}$ this results in a factor of 6 in the resolution requirements compared to $Re = 3900$ [17]. Also, in azimuthal direction a much finer grid has to be employed. Due to the refined grid the critical time step decreases which further increases the cost. Consequently, we have to
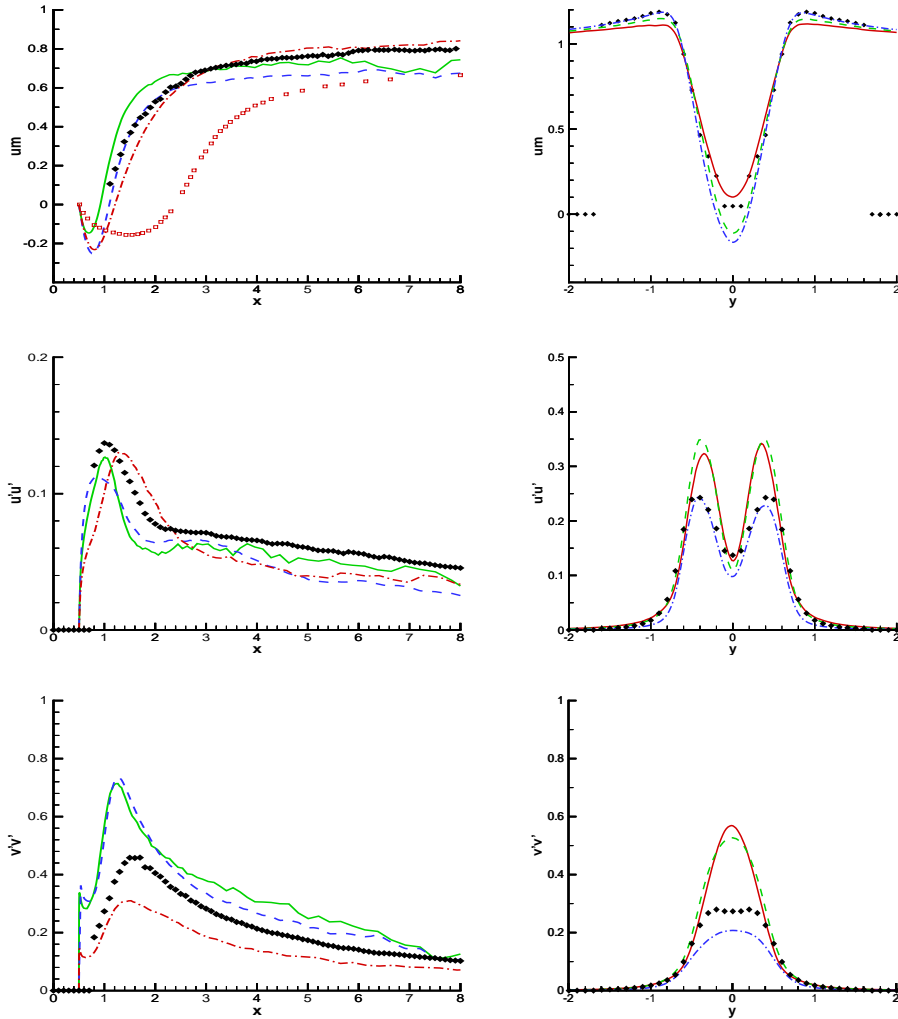

Figure 4 LES of flow around cylinder at $Re = 140000$. Mean streamwise velocity u and Reynolds stresses $\langle u'u' \rangle$, $\langle v'v' \rangle$ along the centerline $y = 0$ (left) and on a line $x = 1$ (right). In all plots ——— RUN 1, $- - -$ RUN 2, $- \cdot - \cdot -$ Run 3. Comparison with experimental results of [9] (full diamond) and an unsteady $k - \varepsilon$ computation of [15] (light square).

be content with fewer computations and less averaging in time. Two–dimensional studies were performed in order to construct grids that meet best the requirements with the available resources. To enhance the resolution of the boundary layer any stretching in azimuthal direction was dropped and the number of points in this direction increased. In [17] we have presented a first LES for this case with $L_z/D = 1$. Two further computations have now been performed with $L_z/D = 4$, motivated by the observed correlation in z and studies of the square cylinder [35]. They are summarized in Table 1. Other computations are available in [7] and [42]. In [42] the authors observe that very long averages of the order of 40 shedding cycles might be required for fully converged statistics. Due to limited resources we could only average over 10–14 cycles. Nevertheless, the performed computations give valuable information on trends and sensitivities. In [7] no superiority of the dynamic model with respect to the Smagorinsky model used in the present LES has been observed.

Figure 4 reports profiles along the centerline $y = 0$ and $x = 1$ for various quantities. It is apparent that in RUN1 the vortex shedding is too strong. As a consequence the maxima of the mean streamwise velocity are less pronounced and the v–fluctuations are over–predicted. Increasing the domain size to $L_z = 4$ with the same number of grid points, i.e. a coarser grid in z, yields only minor changes. An exception is the mean centerline velocity which levels off at a substantially lower value. The third run has been made with an increased resolution in all directions. The resolution of the shear layer is now substantially better which is reflected by the improved result for $\langle \bar{u} \rangle (x = 1)$ outside the recirculation. The Reynolds stresses are substantially lower which is the right tendency (the reported stresses are the resolved ones to which a subgrid scale contribution has to be added). On the other hand the values for C_D, $- C_{bp}$ are too small. We conjecture that the discrepancy results from insufficient resolution of the separating shear layer. The importance of this issue has recently been highlighted in [22] for $Re = 3900$. As in [7], we observe too large separation angles compared to the experiments which is also of relevance for the downstream shear layer. This occurs although the radial resolution in our LES is $\Delta r_1 = 0.00017$ compared to 0.0004 in [7]. The cited computations in the literature have mostly been made with a smaller spanwise domain size. Our results show that increasing L_z does not modify the result substantially. The resolution in radial and azimuthal direction rather appears to be the limiting factor in the present cases. On the other hand, substantial refinement in these directions in [7] did not yield a clear uniform improvement of the result. Interestingly, the best agreement with experiments was obtained with $L_z/D = 1$. We shall continue to work on modelling issues as discussed below in order to possibly obtain an improved and more cost–effective LES of this case.

4   Circular cylinder in presence of shear

4.1   Physics of the flow

Uniform upstream conditions constitute the classical setting for the study of the flow around cylinders. In practice, however, the upstream flow is often non–uniform. Of particular interest is a gradient in spanwise direction as it disrupts the spanwise symmetry of the configuration and generates qualitatively new features [45]. Applications are in the area of buildings placed in the earth's boundary layer, vehicle aero- and hydrodynamics and industrial flows.
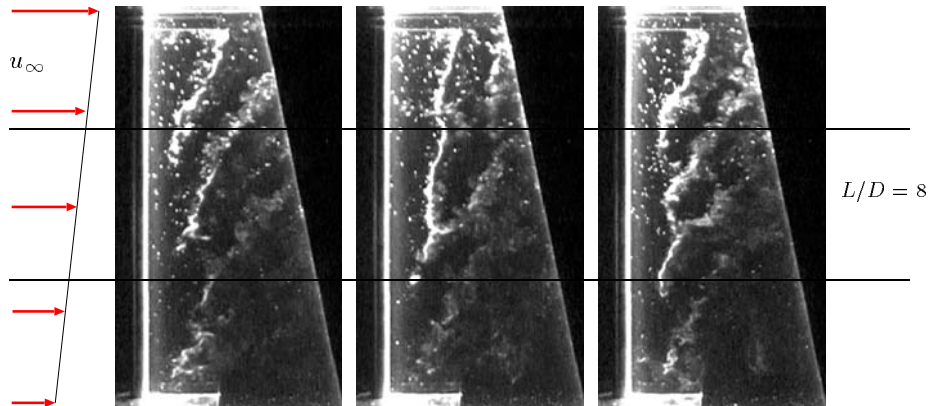
Figure 5 Flow visualization of the vortex shedding behind a circular cylinder in uniform shear flow at $Re_m = 6250$, pictures from [20]. Light regions show hydrogen bubbles trapped in like–sign vortices crossing a laser sheet in the centerplane. There is no temporal correlation between the snapshots. The aspect ratio is $L/D = 20.1$ in the experiment. The aspect ratio $L/D = 8$ of the LES is indicated by two lines.

Reviews on a circular cylinder in uniform spanwise shear are given in [18], [45]. The characteristic parameter is the dimensionless gradient $\beta = du_\infty/dz$, where, as above, cylinder diameter D and average free–stream velocity U_m are used as reference quantities. The gradient causes a variation in the stagnation pressure along the span which in turn generates a secondary flow in front of the body and even more so in the rear (cf. Fig. 7 below). This yields a complicated three–dimensional flow structure interacting with the vortex shedding. An important finding in the experiments with $\beta \neq 0$ such as [32] is that the Strouhal number $St = fD/U_\infty$ does not adjust continuously to the free stream velocity. Rather, the dominant frequency exhibits cells of uniformity. The origin of this behaviour is not entirely clear up to now. Woo et al. [44] have conducted experiments with slotted end plates which inhibit the secondary flow to a smaller extent than the solid end plates in other experiments. They found decreased cell structure. Balasubramanian et al. [2] analyzed these results and conjectured that the strength of frequency cells is closely related to end conditions. The interaction between the three–dimensional average flow and the instantaneous shedding process is not yet understood [45].

4.2   Computational setup

Until now, cylinders in shear flow have mainly been investigated experimentally. RANS models are expected to have similar problems as for uniform upstream flow. Here, LES has a high potential. Recent investigations by means of DNS have been conducted for Reynolds numbers $Re_m = DU_m/\nu$ up to 200 [26],[25].

The present computations deal with the flow at a substantially higher Reynolds number in a configuration which parallels the experiments by Kappler and Rodi [20], [21]. Fig. 5 displays the oblique vortex shedding generated by the shear flow. Characteristic is the occurence of Y–shaped vortex dislocations with the points of junction propagating from the high–speed end to the low–speed end. The experiment in Fig. 5 has been conducted at $Re_m = 6250$, $\beta = 0.04$ and an aspect ratio of $L/D = 20.1$. Since an LES for this geometry
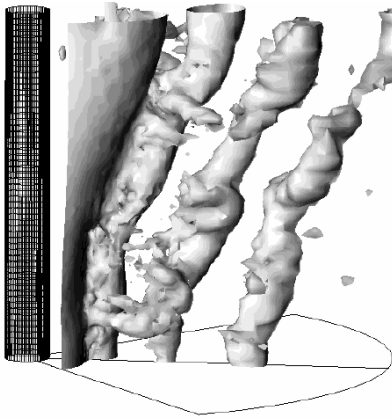
Figure 6 Instantaneous iso–pressure surface $p = -0.6$ in the rear of the cylinder. In angular and radial direction only part of the domain is represented.
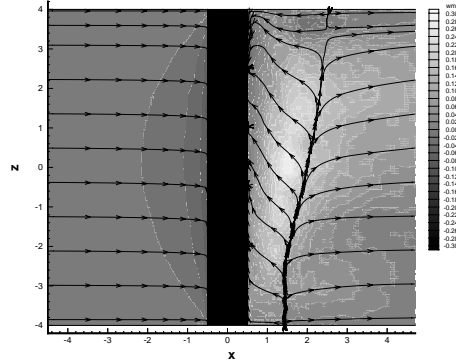
Figure 7 Average flow field in the center plane for cylinder in shear flow: streamlines in the $x - z$ plane and average spanwise velocity depicted by grey scale.

was unaffordable with the available resources the aspect ratio was reduced to $L/D = 8$. The code LESOCC was used with the same numerical scheme as above. This is motivated by the typical extent of the frequency cells mentioned above of around $4D$, so that ideally 2 cells would be generated in this domain. This was confirmed in a later experiment [21] under the same conditions but with $L/D = 8$. Guided by the experience from the earlier LES at $Re = 3900$, an O-grid of diameter $30D$ was employed with $178 \times 176 \times 174$ internal cells in radial, azimuthal and spanwise direction, respectively. Points were clustered in the wake and at the cylinder surface. Laminar inflow was prescribed with $u_\infty = 1 + \beta z$ and a convective outflow condition was used. At $z = \pm 4$ a free slip condition was imposed. It represents at best the effects of the end plates with sidelength $8D$ in the experiment. The effect of the employed Smagorinsky subgrid–scale model is only small since $\nu_t/\nu \leq 1.5$. After a transient phase, the computation has been conducted for 220 time units, i.e. 46 shedding cycles. Time signals were collected at $x = 2.5, y = 0.5, z = 0.4n$, where $n = -10 \ldots 10$ (the outermost at $z = \pm 3.9$), similar to the locations in the experiment. Another computation with $\beta = 0$ has been performed under exactly the same conditions for comparison. Discussion and results in addition to the ones presented below can be found in [16].

4.3 Computed flow field

Figure 6 shows a calculated pressure surface of the instantaneous flow. Closely behind the cylinder the vortex core is parallel to the cylinder axis. Further downstream the von Karman vortices become oblique due to the average shear. The angle which is formed is clearly visible. Braid–like structures connecting the von Karman vortices can be discerned as well.

Figure 7 depicts the computed secondary mean flow discussed above. The spanwise component $\langle \overline{w} \rangle$ increases up to 0.26. The streamlines of the average flow in the center-
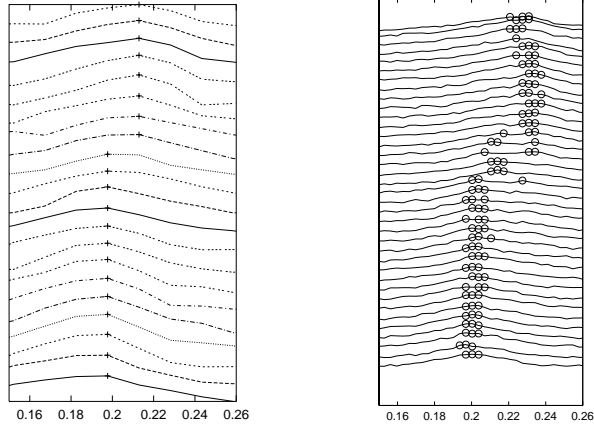
Figure 8 Spectra of the v−velocity signal. Left: results from the present LES with maxima marked by crosses, right: experimental data from [21]. The frequency axis is normalized to represent the Strouhal number. The spectra at different locations have been shifted upwards according to their z−coordinate.

plane highlight the complex three−dimensional character of the flow. They barely display uniformity in z around mid−span and exhibit substantial variations in z at the upper and lower end. Also note the secondary recirculation zone formed at the upper end behind the cylinder.

4.4 Fourier analysis of time signals

The spectra of the velocity signals recorded in the wake have been computed. They exhibit a peak at the dominant shedding frequency and an inertial range over about one decade [16]. Figure 8 shows a zoom around the dominant frequency and compares the LES result to the experimental data for the same configuration [21]. The same cells as in the experiment are observed.

Since, unlike in the experiment, in the LES the time signals have been stored simultaneously at the different locations the correlation coefficient ρ_{ij} between two signals at z_i and z_j can be determined. We have defined a correlation length $l(z_i) = \Delta z \sum_j \rho_{ij}$, $\Delta z = 0.4$, to display this information in Figure 9. In the case without shear l is larger than half the domain size around mid−span and decreases away from it due to the presence of the boundaries. With $\beta = 0.04$ three distinct regions are observed with almost constant value. In particular, the correlation drops towards mid−span where the jump in the shedding frequency occurs in Figure 8. The lower spanwise correlation observed here results in a lower amplitude of the fluctuations of the lift coefficient. Indeed, these are only half as large for $\beta = 0.04$ compared to $\beta = 0$ [16].

4.5 Wavelet analysis of time signals

The above spectra and correlations constitute valuable statistical information but give only an indirect picture of instantaneous mechanisms. This requires time−local averaging as performed with the continuous wavelet transform (CWT) [19], [14]. Further quantities can be defined based on this approach to address particular issues as detailed below.
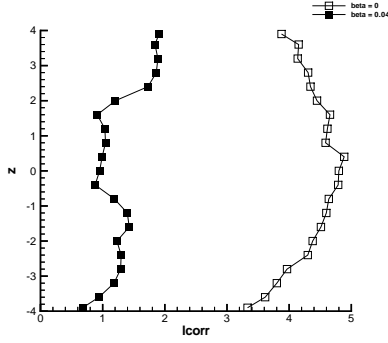
Figure 9 Correlation length l as defined in the text at different spanwise positions. Open symbols: $\beta = 0$, full symbols: $\beta = 0.04$.
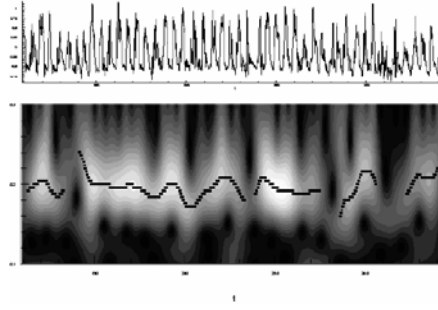
Figure 10 Time signal of v at midspan with $\beta = 0.04$ and its wavelet analysis. The ordinate s is scaled to correspond to the Strouhal number and covers the range $[0.1, 0.3]$. The ridge is only retained if $|W(s_R, t)|$ is larger than 80% of the average of $|W|$ along the ridge.

Any function $\psi(t)$ with Fourier transform $\widehat{\psi}$ and $c_\psi = \int_\infty^\infty |\widehat{\psi}(\omega)|^2/|\omega|d\omega < \infty$ can be used to define a wavelet transform

$$W_f(s,t) = \int_{-\infty}^{\infty} f(t')\, \psi_{s,t}^*(t')dt'. \tag{4.1}$$

Here, dilated and translated versions of ψ are denoted

$$\psi_{s,\tau}(t) = \sqrt{s}\, \psi\left(s(t-\tau)\right) \tag{4.2}$$

while the asterisk stands for the complex conjugate. Oscillating signals are conveniently analyzed with complex wavelet such as the one of Morlet with

$$\psi(t) = \pi^{-1/4}\big(e^{i\omega_0 t} - e^{-\omega_0^2/2}\big)e^{-t^2/2} \tag{4.3}$$

and $\omega_0 = 5$. The transform W then also is a complex value. The scale parameter s plays the same role as the frequency in Fourier analysis and is normalized here so as to correspond to the Strouhal number at which $|\widehat{\psi_{s,\tau}}(\omega)|$ attains its maximum. The value $|W(s,t)|^2$ hence represents the energy of the signal f at time t around the frequency s. If s_R represents the scale number at which $|W(s,t)|^2$ has a maximum for a given time t, the curve $s_R(t)$, the so–called ridge, is an instantaneous analogon of the time–averaged dominant frequency above.

In the following we concentrate on the normal velocity component as it is most directly related to the shedding process. Figure 10 displays a v−signal and its CWT together with the ridge. The frequency range has been chosen in the vicinity of the Strouhal number. It is obvious, that at irregular instances an interrupt or defect in the vortex shedding causes the energy on scales $St \approx 0.2$ to collapse. We therefore retain the ridge only if $|W|$ exceeds a threshold value. A result of this investigation is that the instantaneous shedding frequency hardly ever remains constant for more than 3–4 cycles but rather fluctuates, as reflected by the undulations of the ridge, with a typical period of 5–6 cycles. Without shear $(\beta = 0)$ these undulations are much less pronounced in amplitude and have a slightly shorter period, cf. Figure 12.
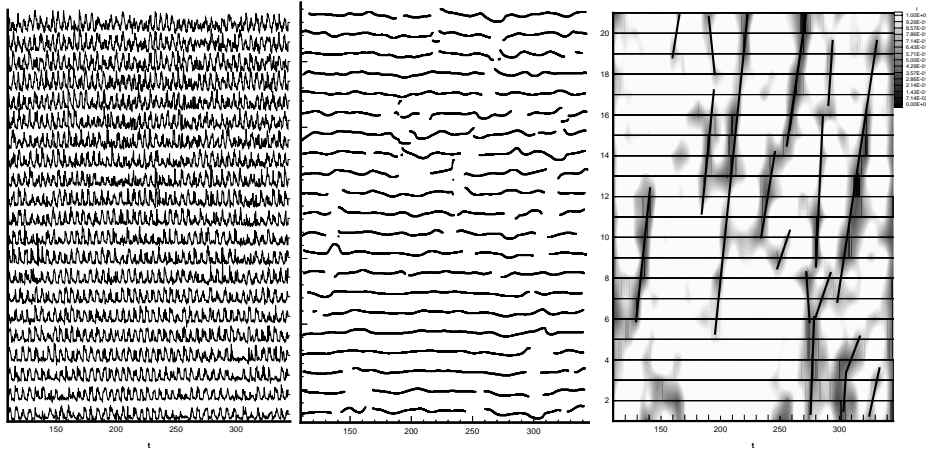
Figure 11 Signals, ridges and intermittency coefficient for $\beta = 0.04$. The horizontal axis is time, the vertical axis is the spanwise position of the signal. Left: v–signals. Middle: ridges as discussed in the text. The shift in the vertical coordinate s between the ridges is 0.15. Right: Intermittency factor I for $St = 0.2$. The continuous distribution between the signals results from the interpolation of the graphics tool. To bring out more clearly the minima of I the gray scale has been squeezed to the lower third of the range in each case. The straight lines have been inserted by hand.
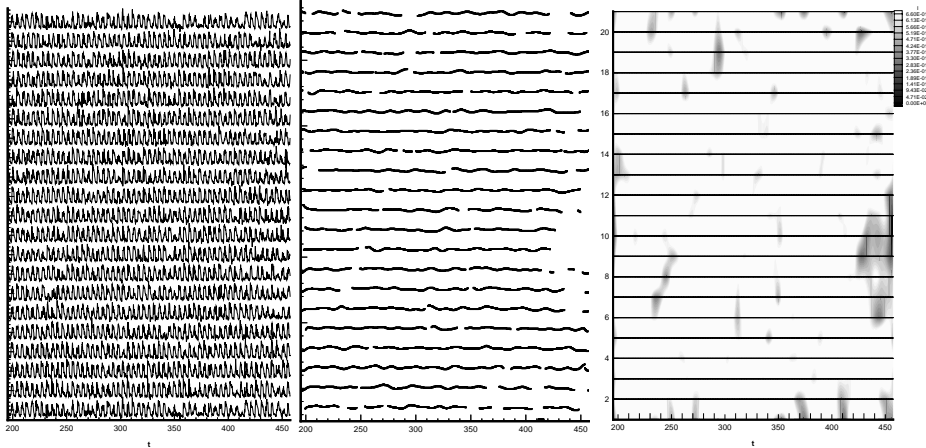

Figure 12 Signals, ridges and intermittency coefficient for $\beta = 0$. For caption see Figure 11.

The defects mentioned above are related to an instantaneous decrease in $|W|$. Since W is a smooth function (cf. Figure 10) s can be kept constant when addressing this issue so that the intermittency coefficient [14]

$$I(s,t) = \frac{|W_f(s,t)|^2}{\langle |W_f|^2 \rangle} \tag{4.4}$$

with $\langle . \rangle$ denoting time averaging is an ideal quantity for their detection. Figure 11 and 12

display $I(0.2,t)$ for all signals. It turns out that with $\beta = 0.04$ defects are stronger than without shear. Furthermore, they propagate from the low–speed end to the high–speed end. Lines have been inserted in the figure by hand in order to estimate their speed yielding a non–dimensional average of about 0.16. The original signals are displayed also. Although here and there defects can be detected by hand, the intermittency coefficient gives a simple and robust means for their determination.

Finally, the CWT can be employed to investigate which events contribute to the Reynolds stresses. The idea is based on the observation that for a complex wavelet [28]

$$\int_{-\infty}^{\infty} f(t)\ g(t)\ dt = \frac{1}{c_\psi} \int_0^\infty \int_{-\infty}^{\infty} C_{fg}(s,t)\ dt\ ds \qquad (4.5)$$

where $C_{fg}(s,t) = R\{W_f(s,t)\ W_g^*(s,t)\}$ is the so–called wavelet co-scalogram and R designates the real part. Now, if f and g are different components of the velocity vector the total Reynolds stress can be obtained by integrating over C_{fg}. Hence, $C_{fg}(s,t)$ indicates which scales and times contribute to the Reynolds stress. Figure 13 shows as an example the $vw-$correlation at midspan. The intermittent generation of the Reynolds stress is visible. Furthermore, there appears to be a drastic change in the phase around $s = 0.2$ in the case with shear compared to the one without shear.

In [16] a similar method is proposed to investigate two–point correlations and phase shifts taking signals at different location for f and g in (4.5). It turns out that the observed defects are accompanied by large phase differences between adjacent signals. Further investigations along the above lines should be carried out to fully exploit the potential of the approach.
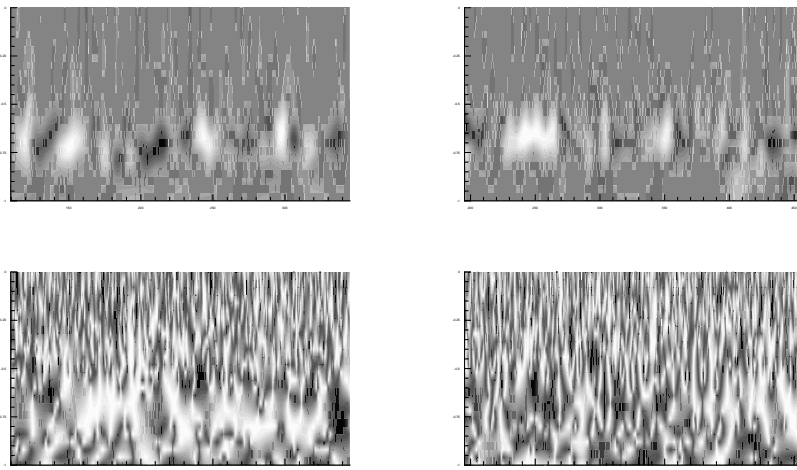

Figure 13 Instantaneous and scalewise correlation between the $v-$ and the $w-$signals at midspan. Horizontal axis is time, vertical axis is $\log(s)$, $s = 0.1\ldots1$. Left: $\beta = 0.04$, right: $\beta = 0$. Top: C_{vw} as defined in the text, scale from -0.0009 to 0.0008. bottom: angle between W_v and W_w in absolute value, light is $90°$, dark is $0°$.

5   Boundary condition by means of an integral method

The computations of flow around circular cylinders described above were made for Reynolds numbers in the sub–critical regime where the boundary layer along the cylinder wall remains laminar until separation. Transition to turbulence occurs after separation in the shear layers. Resolving the boundary layer becomes increasingly difficult as the Reynolds number increases and requires a finer and finer mesh. We have therefore developed a model for the windward boundary layer and implemented it in the LESOCC code. It is based on an integral method and allows a coarser discretization normal to the wall yielding savings in CPU time and memory.

The laminar boundary layer is unsteady as it is shifted around the cylinder by the vortex shedding. This motion, however, is small and slow compared to the internal time scale of the boundary layer: Dwyer, McCrosky [13] measured an amplitude of 3.7° for the oscillation of the stagnation point for $Re = 1.06 \cdot 10^5$ and in [31] the criterion $St < 14$ is derived for the second property to hold (here, $St \approx 0.2$). The instantaneous velocity profiles in the boundary layer at a certain distance from the stagnation point hence correspond to the steady state profiles at this distance from the average stagnation point and the laminar boundary layer is amenable to a quasi–steady description.

Integral methods represent a boundary layer in terms of integrals over its thickness such as the displacement thickness δ^*, or the momentum thickness θ. The method of Thwaites [10] is one of them based on the empirical relation

$$\frac{u_e}{\nu}\frac{d\theta^2}{ds} = F(\lambda) = A + B\lambda \quad ; \quad A = 0.45 \quad ; \quad B = 6 \quad , \tag{5.6}$$

where $\lambda = \theta^2 \frac{du_e}{ds}/\nu$, s the tangential coordinate, and u_e the external velocity in the direction of s. Integration in closed form is possible yielding

$$\theta^2(s) = \frac{1}{u_e^B}\int_{s_0}^{s} A\,\nu\,u_e^{B-1}\,ds\ + u_e^B(s_0)\,\theta^2(s_0) \quad . \tag{5.7}$$

The last term vanishes if s_0 is a stagnation point. Eq. (5.6) can be used for $\lambda \in [-0.1; 0.1]$ with $\lambda = -0.09$ corresponding to separation. The shear stress is subsequently obtained by an empirical correlation for $S(\lambda) = c_f\,u_e\,\theta/(2\nu)$, and δ^* is obtained from a similar correlation for the shape factor $H(\lambda)$ [10].

The implemented algorithm proceeds as follows: a one–dimensional problem along a line of constant z is generated. This is straightforward due to the structured O–grid. Actually, the method is applied to the mean flow so that only one such problem has to be solved. Next, the stagnation point s_0 is determined as a zero crossing of the tangential velocity. Then u_e in (5.7) is replaced by $\sqrt{2(p_w - p_0)/\rho}$. Using the wall pressure is advantageous as it avoids to determine the location of u_e, particularly difficult for medium Reynolds numbers. Eq. (5.7) is then integrated from s_0 until $\lambda < 0.095$, i.e. shortly beyond separation where θ and δ^* drastically increase.

The basis for using the above method in an LES is Schumann's relation [38]

$$\tau_\omega = \frac{\langle\tau_\omega\rangle}{\langle\overline{u}_1\rangle}\overline{u}_1 \quad , \tag{5.8}$$

where $\overline{u}_1$ is the tangential velocity at the wall–adjacent grid point. The integral method applied to the mean flow yields $\langle\tau_\omega\rangle$. With (5.8), local variations are accounted for by the

relation to $\overline{u}_1$. Eq. (5.8) furthermore allows to blend this method with a no–slip condition which can be put in the same form. This is performed depending on the resolution of the boundary layer, measured by the coefficient $\Delta r_1/\delta^*$. If the latter is small, the radial resolution is good and a no–slip condition is adequate (Fig. 14).

Tests have been performed in the two–dimensional setting for $Re = 140000$. Recall that the physics of the wake are substantially different in this case compared to 3d, but the windward laminar boundary layer remains almost unaffected. Figure 14 shows the computed boundary layer thickness until separation and the resulting wall–shear stress along the circumference of the cylinder. Three–dimensional LES with this model will be performed in the near future. Note that with (5.8) blending to other wall models can easily be performed by choosing a different way to determine $\langle\tau_\omega\rangle$ [16]. The method can also be extended to turbulent boundary layers when replacing the method of Thwaites by another, appropriate integral method.
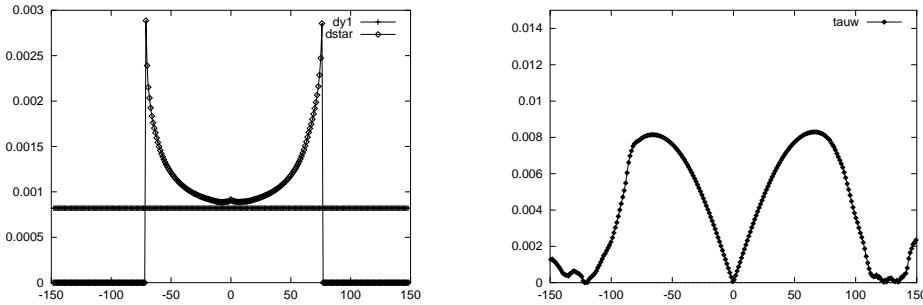

Figure 14 Determination of the wall–shear stress on the windward face with Thwaites' method as described in the text. Left: δ^* and Δr_1, the size of the wall adjacent cell in radial direction, versus the azimuthal angle. Right: computed wall–shear stress with blending to a no–slip condition used.

6   Investigation of a variable filter size

In complex flows the mesh size of the employed grid cannot be kept constant as envisaged in the classical concept of LES. This also applies to the above computations of the flow around cylinders requiring substantial refinement near the surface of the body. The cutoff scale then varies in space and interacts with the turbulence modelling. This can be appreciated best when considering a flow with a statistically homogeneous direction. Varying the mesh size and hence the filter width in this direction introduces a statistical inhomogeneity of the resolved flow. To isolate the effect we consider developed channel flow and apply a streamwise non–uniform grid. In [17] LMFA contributed a computation in which an abrupt change of the mesh size was modelled. We have now performed a closer comparative study of this phenonenom by means of plane channel flow at $Re_b = 10935$ for which a DNS is reported in [1]. An LES using the LESOCC code was perfomed on a grid with a gradually varying streamwise step size and streamwise periodicity (Figure 15). It contains two regions of constant step size, $\Delta x^+ = 220$ and $\Delta x^+ = 30$, respectively, limited by two intermediate zones with 5% geometric stretching. The dynamic model

is used with averaging in spanwise direction and temporal relaxation [8]. The Werner-Wengle wall model is used to bridge the distance between the first point at $y_1^+ = 30$ and the wall, furthermore $\Delta z^+ = 30$. For the same grid LMFA performed a computation with the statistical two–point closure S.C.I.T. [30] which has, compared to the study reported in [17], now been generalized for anisotropic turbulence [41] and is briefly described in Appendix A. The S.C.I.T. method is usually applied to model the entire spectrum, but for the application to the problem of subgrid–scale modelling a spectral cut off $K < K_c$ is introduced. The contribution $K > K_c$ is then modelled by a spectral eddy viscosity

$$\nu_{t_c} = \left(C_1 + C_2 \left(\frac{K}{K_c} \right)^{C_3} \right) \sqrt{\frac{E(K_c)}{K_c}} \tag{6.9}$$

with $C_1 = 0.267$, $C_2 = 0.4724$, $C_3 = 3.742$ as proposed in [11]. To represent the size of the computational grid the cutoff wavenumber K_c is set proportional to $1/\Delta_x$.

Figure 15 shows $< u'/u_\tau >^2$ on a cut along the centerline of the channel. The streamwise mesh size of the grid is marked by crosses. It is obvious that both methods, although entirely different in their approach, give a very similar result. In accordance with the filtering underlying an LES the resolved stress is smaller in regions of the coarse grid and higher in regions of the fine grid. Instructive, however is the observed relaxation in zones of constant mesh size after the stretching or shrinking. When the grid is coarsened, the effect of filter becomes more and more pronounced. There, the energy loss appears to be roughly proportional to the mesh size. The settling in the subsequent area of constant mesh size is a little less pronounced with the LES method than with S.C.I.T. When the grid is refined energy has to be supplied to the newly added resolved fine scales by the turbulence cascade. This process is slow compared to the time it takes a particle to advance into a region of finer grid, although the stretching rate is only 5%. The resolved stress increases slower than it decreased before and a substantial relaxation is observed. In fact, the zone of constant fine grid has to be larger to achieve complete relaxation, but this would have increased the cost of the LES substantially. It should be recalled that in an a priori test when filtering a fully resolved flow field with a variable mesh size the stresses would follow exactly the step size of the grid. This is not the case here due to the dynamic process described above. It is illustrative to mirror the distribution which corresponds to a reversed flow direction (Figure 15 right) to support the above remarks.

The performed computations demonstrate that coarsening the grid in streamwise direction has much less effect than refining the grid. Indeed, the latter appears to be detrimental to current subgrid-scale modelling. In the above bluff–body flows we are only faced with the former, since the refinement of the grid takes place in the laminar part of the flow. Research will be pursued in order to possibly develop a correction to standard subgrid-scale models which compensates the observed phenomenon.

7   Concluding remarks

The present paper assembles various activities of the cooperation between the German and the French partners. They concern the numerical aspect in that a structured and two unstructured codes have been employed for the same flow. In particular, the resolution requirement which is extremly demanding for the higher Reynolds number case is discussed. A proposal for a boundary layer model to be integrated in such an LES
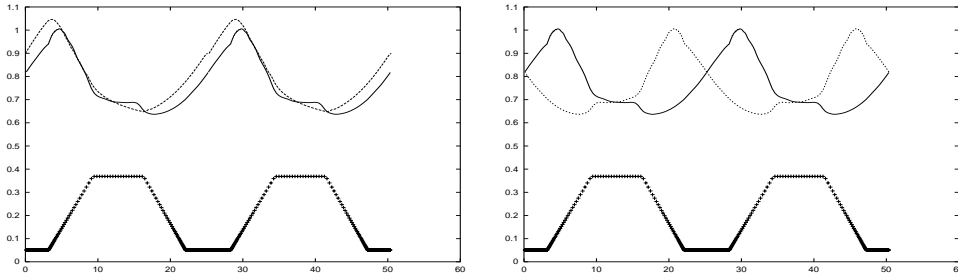
Figure 15 Reynolds stress $< u'/u_\tau >^2$ on the centerline of a channel with variable streamwise grid spacing as described in the text (+). The computation was performed for one period [0,25.1], which is repeated in the figure to enhance clarity. Right: comparison between results of S.C.I.T. ($- - -$) and the LES performed with LESOCC (——). Left: plot of LES result (——) together with the same data for a reversed flow direction ($- - -$).

of a subcritical cylinder has been made to alleviate this problem. The approach can be extended for turbulent boundary layers as well. A more physical study has been undertaken with the computation of the flow around a cylinder in uniform shear flow at a much higher Reynolds number than considered in the current literature. For this purpose, analyzing techniques have been developed which take into account variations in the instantanous character of the signal. They reveal defects in the regular vortex shedding which propagate in spanwise directions and appear more frequently in the presence of spanwise shear. The implemented algorithms can partly also be applied to the available experimental time signals, and this will be done in future work. Finally, the model study of streamwise grid refinement highlights the methodological problems this may create. Although this issue is pertinent to many cases where LES is applied to complex flows it has to our knowledge not been investigated in detail up to now. We will continue work on this issue as it seems to be desirable that an SGS model should account for such effects.

Acknowledgments

Appendix A: Turbulence model employed by LMFA

The S.C.I.T. model (for Simplified Closure for Inhomogeneous Turbulence) [30] is based on a statistical spectral approach, that is to say on a description of turbulence by correlations at two points. It is known that two–point models directly take into account information on different length scales, up to the Kolmogorov scale. Consequently no ϵ equation is required. Before being applied to real flows, the complex formulations of two–point closures for inhomogeneous turbulence must however be simplified. This is the

approach followed when developing the S.C.I.T. model.

A first version of the S.C.I.T. model (S.C.I.T.0) was proposed in [30]. The basic quantity in S.C.I.T.0 is the turbulent kinetic energy spectrum $E(K,\vec{X},t)$ and consequently, although a detailed spectral information was retained, the anisotropic properties of turbulence are only grossly accounted for. The next stage was to extend the approach to a tensorial description of the turbulent spectra

$$\varphi_{ij}(K,\vec{X},t) = \int_{|\vec{K}| \leq K} \Phi_{ij}(\vec{K},\vec{X},t)\,d\sigma(\vec{K}) \quad , \tag{8.10}$$

with $\Phi_{ij}(\vec{K},\vec{X},t)$ being the Fourier transform on the correlation $\langle u_i(\vec{x}-\vec{r}/2)\,u_j(\vec{x}+\vec{r}/2)\rangle$ and K the modulus of $\vec{K}$. It results in a new version of the model (S.C.I.T.1) [41] which is applied here. The equation for φ_{ij} reads:

$$
\begin{aligned}
\left(\frac{\partial}{\partial t} + \langle U_e\rangle \frac{\partial}{\partial X_l}\right)\varphi_{ij}(\vec{X},K,t) &= \left(-2\nu K^2 + \frac{\nu}{2}\nabla^2\right)\varphi_{ij}(\vec{X},K,t) \\
&\quad + P_{ij}(\vec{X},K,t) + p_{ij}^L(\vec{X},K,t) \\
&\quad + p_{ij}^{LW}(\vec{X},K,t) + t_{ij}^L(\vec{X},K,t) \\
&\quad + t_{ij}(\vec{X},K,t) + D_{ij}(\vec{X},K,t) \quad ,
\end{aligned}
\tag{8.11}
$$

in which the first term of the right hand side is a viscous contribution which can be expressed exactly. The second term P_{ij} is also a term which is not requiring a closure (production term). The other terms $p_{ij}^L, p_{ij}^{LW}, t_{ij}^L, t_{ij}$ and D_{ij}, respectively, stand for the rapid part of the pressure–strain spectrum, the echo term associated with wall effects, the linear transfer, the non linear transfer and the inhomogeneous transport term. These terms were closed introducing various assumptions described in [41]. One of the basic ingredients in the model is the use of the EDQNM theory to express the transfer term [29]. The relation between S.C.I.T.0 and S.C.I.T.1 is illustrated by the relation $E(K,\vec{X},t) = 1/2\varphi_{ii}(K,\vec{X},t)$. Correspondingly, in S.C.I.T.0 only a transport equation for E is solved.

The computation procedure consists in discretizing the K-space, and in solving at each wave length K the six equations for φ_{ij} on the physical computational domain. Then, one gets the information required to close the averaged Navier-Stokes equations, which are solved together with (8.11):

$$\langle u_i u_j\rangle = \int_0^\infty \varphi_{ij}(K,\vec{X})\,dK \quad . \tag{8.12}$$

Concerning the near wall treatment, a spectral "infrared cut-off", depending on the distance to the wall is imposed as in [30]. For the pressure strain correlation, an echo term is introduced. The boundary conditions for the different turbulent quantities are deduced from wall functions. A log law is assumed and a hyperbolic tangent profile is used to match with the viscous sublayer [12].

References

[1] AGARD, Neuilly–sur–Seine, France. *A selection of test cases for the validation of Large Eddy Simulations of turbulent flows*, 1998.

[2] S. Balusubramanian, F.L. Haan Jr., A.A. Szewczyk, and R.A. Skop. On the existence of a critical shear parameter for cellular vortex shedding from cylinders in nonuniform flow. *J. Fluids & Struct.*, 12:3–16, 1998.

[3] P. Beaudan and P. Moin. Numerical experiments on the flow past a circular cylinder at sub–critical Reynolds number. Technical Report TF-62, Stanford University, 1994.

[4] U. Bieder. PRICELES: Large Eddy Simulation of the very near wake of a circular cylinder. Technical Report DRN/DTP/SMTH/LATA/99-73, CEA Grenoble, 1999.

[5] U. Bieder. PRICELES: Tests of the numerical scheme. Technical Report DRN/DTP/SMTH/LATA/99-52, CEA Grenoble, 1999.

[6] U. Bieder, Ph. Emonot, and D. Laurence. PRICELES: Summary of the numerical scheme. Technical Report DRN/DTP/SMTH/LATA/98-50, CEA Grenoble, 1998.

[7] M. Breuer. A challenging test case for Large Eddy Simulation: High Reynolds number circular cylinder flow. In S. Banerjee and J.K. Eaton, editors, *Turbulence and Shear Flow Phenomena – 1*, pages 735–740, New York, 1999. Begell house inc.

[8] M. Breuer and W. Rodi. Large eddy simulation of complex turbulent flows of practical interest. In E.H. Hirschel, editor, *Flow simulation with high performance computers II*, volume 52 of *Notes on Numerical Fluid Mechanics*, pages 258–274. Vieweg, Braunschweig, 1996.

[9] B. Cantwell and D. Coles. An experimental study of entrainment and transport in the turbulent near wake of a circular cylinder. *J. Fluid Mech.*, 136:321–374, 1983.

[10] T. Cebeci and P. Bradshaw. *Physical and Computational Aspects of Convective Heat Transfer*. Springer Verlag, New York, 1984.

[11] J.P. Chollet and M. Lesieur. Parameterization of small scales of three dimensional isotropic turbulence. *J. Atmos. Sci.*, 38:2747–2757, 1981.

[12] P. Debaty. *Performances des modèles de turbulence au second ordre appliqués à des configurations axisymétriques simulées par éléments finis*. PhD thesis, École Centrale de Lyon, 1994.

[13] H. Dwyer and W.J. McCroskey. Oscillating flow over a cylinder at large Reynolds number. *J. Fluid Mech.*, 61:753–767, 1973.

[14] M. Farge, N. Kevlahan, V. Perrier, and E. Goirand. Wavelets and turbulence. *Proceedings of the IEEE, Special Issue on Wavelets*, 84:639–669, 1996.

[15] R. Franke. *Numerische Berechnung der instationären Wirbelablösung hinter zylindrischen Körpern*. PhD thesis, Universität Karlsruhe, 1991.

[16] J. Fröhlich. LES of vortex shedding past circular cylinders. to appear in Proceedings of ECCOMAS 2000, Barcelona, 11–14 September, 2000.

[17] J. Fröhlich, W. Rodi, Ph. Kessler, S. Parpais, J.P. Bertoglio, and D. Laurence. Large eddy simulation of flow around circular cylinders on structured and unstructured grids. In E.H. Hirschel, editor, *Notes on Numerical Fluid Mechanics*, volume 66, pages 319–338. Vieweg, 1998.

[18] O.M. Griffin. Vortex shedding from bluff bodies in a shear flow: a review. *Trans. ASME: J. Fluids Eng.*, 107:298–306, 1985.

[19] A. Grossman, R. Kronland-Marinet, and J. Morlet. Reading and understanding continuous wavelet transforms. In J.M. Combes, A. Grosman, and P. Tchamitchian, editors, *Wavelets, Time–Frequency Methods and Phase Space*, pages 2–20. Springer, 1989.

[20] M. Kappler and W. Rodi. Experimentelle Untersuchung der Strömung um Kreiszylinder mit ausgeprägten dreidimensionalen Effekten. Technical Report Ro-558/15-1, Institut für Hydromechanik, Universität Karlsruhe, 1998.

[21] M. Kappler, W. Rodi, and O. Badran. Experiments on the flow past a long circular cylinder in a shear flow. In *accepted for presentation at 4th International Colloquium on Bluff Body Aerodynamics & Applications, September 2000, Bochum*, 2000.

[22] A. G. Kravchenko and P. Moin. Numerical studies of flow over a circular cylinder at $Re_D = 3900$. *Phys. Fluids*, 12:403–417, 2000.

[23] L.M. Lourenco and C. Shih. Characteristics of the plane turbulent near wake of a circular cylinder. A particle image velocimetry study. (data taken from Beaudan,Moin(1994)), 1993.

[24] R. Mittal. Progress of LES of flow past a circular cylinder. In *Annual Research Briefs 1996*, pages 233–241. Center for Turbulence Research, 1996.

[25] A. Mukhopadhyay, P. Venugopal, and S. P. Vanka. Numerical study of vortex shedding from a circular cylinder in linear shear flow. *J. Fluids Eng.*, 121:460–468, 1999.

[26] D.J. Newmann and G.E. Karniadakis. A direct numerical simulation of flow past a freely vibrating cable. *J. Fluid Mech.*, 344:95–136, 1997.

[27] L. Ong and J. Wallace. The velocity field of the turbulent very near wake of a circular cylinder. *Experiments in Fluids*, 20:441–453, 1996.

[28] M Onorato, M V Salvetti, G Buresti, and P Petagna. Application of a wavelet cross-correlation analysis to DNS velocity signals. *Eur. J. Mech. B/Fluids*, 16(4):575–598, 1997.

[29] S.A. Orszag. Analytical theories of turbulence. *J. Fluid Mech.*, 41:363–386, 1970.

[30] S. Parpais and J. P. Bertoglio. A spectral closure for inhomogeneous turbulence applied to turbulent confined flow. Kluwer Academic editor, ETC VI, July 1996.

[31] D.E. Paxson and R.E. Mayle. Velocity measurements on the forward portion of a cylinder. *J. Fluids Eng.*, 112:243–245, 1990.

[32] R.D. Peltzer and D.M. Rooney. The effects of roughness and shear on vortex shedding cell lengths behind a circular cylinder. *Trans. ASME: J. Fluids Eng.*, 107:61–66, 1985.

[33] W. Rodi. Comparison of LES and RANS calculations of the flow around bluff bodies. *J. Wind Ind. Aerodyn.*, 69-71:55–75, 1997.

[34] W. Rodi. Large–Eddy Simulation of the flow around bluff bodies. In B. Launder and N. Sandham, editors, *Closure Strategies for Turbulent and Transitional Flows*, volume to appear. Cambridge University Press, 2000.

[35] W. Rodi, J.H. Ferziger, M. Breuer, and M. Pourquié. Status of large eddy simulation: Results of a workshop. *J. Fluid Eng.*, 119:248–262, 1997.

[36] P. Rollet-Miet, D. Laurence, and J.H. Ferziger. LES and RANS of turbulent flow in tube bundles. *Int. J. Heat Fluid Flow*, 20:241–254, 1999.

[37] G. Schewe. On the force fluctuations acting on a circular cylinder in crossflow from sub-critical up to transcritical Reynolds numbers. *J. Fluid Mech.*, pages 265–285, 1983.

[38] U. Schumann. Subgrid scale model for finite difference simulations of turbulent flows in plane channels and annuli. *J. Comput. Phys.*, 18:376–404, 1975.

[39] J. Son and T.J. Hanratty. Velocity gradients at the wall for flow around a cylinder at Reynolds numbers from 5×10^3 to 10^5. *J. Fluid Mech.*, 35:353–368, 1969.

[40] S. Szepessy and P.W. Bearman. Aspect ratio and end plate effects on vortex shedding from a circular cylinder. *J. Fluid Mech.*, 234:191–217, 1992.

[41] H. Touil, S. Parpais, and J. P. Bertoglio. A spectral model for anisotropic inhomogeneous turbulence. 13th Australasian Fluid Mechanics Conference, Monash University, Melbourne, Australia, December 1998.

[42] A. Travin, M. Shur, M. Strelets, and Ph. Spallart. Detached–eddy simulations past a circular cylinder. submitted, 2000.

[43] T. Wei and C.R. Smith. Secondary vortices in the wake of circular cylinders. *J. Fluid Mech.*, 169:513–533, 1986.

[44] H.G.C. Woo, J.E. Cermak, and J.A. Peterka. Secondary flows and vortex formation around a circular cylinder in constant-shear flow. *J. Fluid Mech.*, 204:523–542, 1989.

[45] M.M. Zdravkovich. *Flow Around Circular Cylinders*. Oxford University Press, 1997.